Anatase titania activated by Cu(II) or Zn(II) nanoparticles for the photooxidation of methanol assisted by Rhodamine-B

Wissame Chettah, Siham Barama, Mohamed-Salah Medjram, Mohamed Selmane, David Montero, Anne Davidson, Jacques C. Védrine

Anatase titania activated by Cu(II) or Zn(II) nanoparticles for the photooxidation of methanol assisted by Rhodamine-B.

Wissame Chettah[1], Siham Barama[2*], Mohamed-Salah Medjram[1*], Mohamed Selmane[3], David Montero[3], Anne Davidson[4*] and Jacques C. Védrine[4]

[1]: *Laboratoire de Génie Chimique et Environnement de Skikda (LGCES), Université-20 Août-1955-de-Skikda, B.P.26 route d'El-Hadaiek, 21000, Skikda-Algeria.*
[2]: *Laboratoire Matériaux Catalytiques & Catalyse en Chimie Organique (LMCCCO), USTHB BP32 El Alia Bab Ezzouar, 16111, Algiers-Algeria.*
[3]: Institut des Matériaux de Paris Centre, FR 2482, Sorbonne Université, 4 place Jussieu, 75005 Paris, France
[4]: *Laboratoire de Réactivité de Surface (LRS), Sorbonne Université, 4 place Jussieu, 75252 Paris-France.*

*Corresponding authors: anne.davidson@sorbonne-universite.fr; siham_barama@yahoo.com and medjram_ms@yahoo.fr

---

Abstract.
This paper deals with the photocatalytic reactivity of anatase titania particles, modified by surface deposition of Cu^{2+} and Zn^{2+} oxide/hydroxide nanoparticles which are detected by EDS and FX techniques. The objective of the preparation steps was chosen to avoid the formation of larges Cu and Zn oxide particles, which could be identified by XRD and other techniques. Their activity for methanol photocatalytic oxidation in water was studied and Rhodamine-B was added as photo-sensibilizer. To obtain a-TiO_2 support, a thermal activation of commercial Millennium-PC500 nanosized powder was achieved. 3Cu/a-TiO_2 and 3Zn/a-TiO_2 catalysts (3wt% of Cu or Zn) were prepared under simple, easy and reproducible experimental conditions, namely by impregnation with nitrate salts. Catalysts and titania support were characterized by: X-rays diffraction, fluorescence spectroscopy, FEG-SEM equipped with EDS accessory, N_2-sorption and UV-Vis Diffuse Reflectance spectroscopy. Only crystalline anatase $TiO_2$was identified by XRD and large Cu and Zn oxide/hydroxide nanoparticles were easily evidenced by EDS and other techniques. Electronic band-gap was measured by UV-Vis spectroscopy using Kubelka-Munkand Tauc's methods, results varied in the order: 3Cu/a-TiO_2<a-TiO_2 <3Zn/a-TiO_2; also, the presence of reduced Ti^{3+}cations have been demonstrated by this technique. Two photo-activated reactions take place in parallel, on the one hand the photooxidation of methanol with titania holes, on the other hand photo-generated electrons are formed in the titania conduction band. They can react rapidly with diluted oxygen to generate superoxide radicals or with RhB molecules to generate RhB° radicals. RhB molecules are mainly mono-deethylated. After 150 min of reaction, RhB was 98% degraded with 3Cu/a-TiO_2 best catalyst.

Keywords: *Dye-sensibilizer; Rhodamine-B; Methanol photooxidation; Titania; (Cu,Zn) oxide/hydroxide nanoparticles.*

1. Introduction.

The use of organic dyes-sensitizers is one of the most suitable and convenient pathway for extending the photo-response of TiO_2 in the visible region of sunlight [1-4], because of high sunlight absorption capacity and electrons transport ability of these sensitizers [5]. Rhodamine-B dye (noted RhB) can be used as better photo-sensibilizer in visible-light to activate titania and it have received a considerable attention in recent years [6-10]. RhB has been widely adopted in biotechnology applications such as fluorescence-microscopy, flow cytometry and as a tracer-dye in water to determine volumes and flow rates. This dye is often used in industrial applications such as printing, dyeing in textile [11], paper, paints, leathers,…etc and therefore could constitute a contaminant in textile effluents. On another side, the photocatalytic oxidation of methanol is widely studied as a model for the formaldehyde production [12]. Formaldehyde (HCHO) has a great economic importance and large applications in industrial chemical industries [13-15]; it is also an excellent antimicrobial and disinfection/sterilization agent used in detergents, shampoos and medical offices. In recent years, a large number of studies have dealt with the partial oxidation of methanol for producing formaldehyde by the mean of heterogeneous catalysis, electrocatalysis, photocatalysis and electro-photocatalysis procedures [13, 16, 17]. Currently, in industry, formaldehyde is synthesized by direct gas-phase catalytic oxidation of methanol (a non-clean process) in presence of $FeMoO_4$ heterogeneous catalyst; in contrast, the photocatalytic oxidation of methanol to formaldehyde in aqueous solution is considered as a clean process due to trapping of formaldehyde in water. N. Tabaja et al. [18] mentioned that mechanism of partial photo-oxidation of methanol to formaldehyde can be accompanied by parallel and competitive reactions with final formation of intermediates such as 1C, CO_2 and formic acid and 2C, methyl formate. Many experimental studies have been conducted to study of catalytic photochemistry of methanol in presence of TiO_2-based photocatalyst [12, 19, 20], e.g. TiO_2 (anatase or rutile) and TiO_2 DegussaP-25 type [21-23]. Titanium dioxide is the most common semiconductor used for photocatalytic applications as for water depollution by oxidants (H_2O_2, O_3, O_2) [24-28]. Anatase TiO_2 (with indirect band-gap equal to 3.1-3.3 eV and direct band-gap of 1.7 eV) is active with UV light but rather little active with visible light, but it is possible to improve its optical absorption properties in the visible light region [29, 30]. Several methods [31-34] have been tested for the modification of titanium dioxide to change its charge transfer properties as well as bulk modifications by cationic and anionic doping [35, 36]. However, most of the used inorganic techniques have several disadvantages, such as cost and still weak visible light absorption [37]. For its known feature [38], the use of copper nanoparticles has been considered as a promising option because it has been shown to be an effective co-catalyst to TiO_2 in many photocatalytic reactions in comparison e.g. to noble metals [1, 39-43]. While in the term of impregnation or dispersion on titanium oxide, the zinc element has been very little studied in catalytic photo-oxidative reactions under visible light [44].

In the present work, 3w% of Cu or Zn oxide/hydroxide nanoparticles were introduced by impregnation in the form of aqueous salts solutions on titania. Here, the main objective of

modification of commercial titanium dioxide nanopowder (in order to obtain the support) is to reduce its gap band which could have led to modify its optical response in visible light region.

2. Experimental.

2.1. Support preparation:

Several commercial forms of TiO_2 have been applied for the depollution of water in the presence of sunlight such as AEROXIDE®Evonik P25 (mixtures of anatase and rutile) and Millennium-PCs (PC50, PC100, PC105 andPC500). In this work, a commercial material Millennium-PC500 Inorganic Chemicals (Degussa, TiO_2 anatase) has been selected. The elaborated support was a mixture of two TiO_2 with the same "anatase" allotropic-form but presenting different crystal sizes. The crushed support was prepared by the phase-solid mixing of 80% of uncalcined anatase Millennium-PC500 and 20% of activated or calcined anatase Millennium-PC500 as represented in figure-1. The mono-crystallization modification of Millennium-PC500 consists in its thermal activation at 500°C under air (heating rate: $2°C.min^{-1}$ for 3 h). More accurately, an amount of commercial Millennium-PC500 was calcined in air at 500°C to pre-agglomerate the grains of titania and increase the size of crystallites (e.g. from 47.4 to 118.6 nm, this measured size is perpendicular to (101) plans). The final support (obtained without any calcination) was prepared by grinding weight quantities of 80% of uncalcined Millennium-PC500 and 20% of calcined Millennium-PC500. The mixture of titanium dioxide nanoparticles with anatase crystalline structure was employed as support and noted a-TiO_2.

2.2. Synthesis of catalytic materials:

Copper and zinc nitrates are standard Sigma-Aldrich reagents. 3wt.% loading of Cu^{2+} and Zn^{2+} ions are dispersed on a-TiO_2 in 25 mL of water (ratio: ions/a-TiO_2=0.03/0.97)using strong magnetic stirring (Ceramic-Hotplate Stirrer 230V/50-60Hz, rotational speed: 1500 rpm). The nitrates aqueous solutions of $Cu(NO_3)_2.2.5H_2O$ or $Zn(NO_3)_2.6H_2O$ are prepared and added to the suspension of a-TiO_2 as represented in figure-1. After 3h of stirring, the two solids were centrifuged and washed with distilled water and then dried at 80°C during 12 h. Finally, the two solids were calcined at 450°C under air (heating rate: $2°C.min^{-1}$, for 3h) and noted 3Cu/a-TiO_2 and 3Zn/a-TiO_2 (it can be noted a remarkable change of color from white to light green with copper and off-white with zinc).

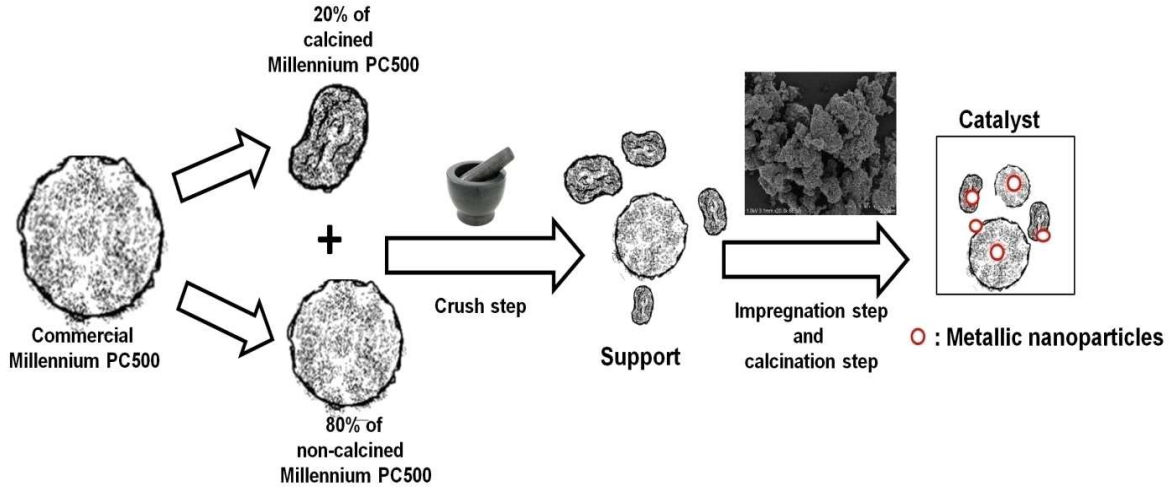

Figure-1. Synthesis steps of each catalyst (SEM image of a-TiO_2 support).

2.3. Photocatalytic test and formaldehyde detection:

The photocatalytic reactor consists of a double-walled 400 mL Pyrex glass beaker (previously washed with 0.1 mol.L^{-1} of NaOH solution before each use). Glassware was equipped with halogen lamp (characteristics: phytotherapy-lamp, 100 watts, HALOPAR-OSRAM-30-ALU, made in Germany) which was immersed in 1/3 inside the photoreactor. The halogen light source works with emission of visible and near-IR radiations. The photocatalytic reactor is equipped to ensure the water circulation. This reactor was connected to large reservoir of water (10 L) maintained at ambient temperature and an efficient circulation of water is provided with a pump for maintaining the temperature of an aqueous solution inside reactor as constant as possible at 24.0 ± 0.2°C).

During the photocatalytic experiments, the reactor was filled with 200 mL of a solution containing 100 mL of Rhodamine-B in water, prepared with a molar concentration of $2.1.10^{-5}$ mol.L^{-1} and a resulting pH value of 4.1, and 100 mL of methanol diluted in water prepared with molar concentration of $2.1.10^{-4}$ mol.L^{-1}. 200 mg of catalyst was suspended into Rhodamine-B solution and magnetically stirred during 60 min. The q_e adsorptive capacity (g.g^{-1}) in dark (dark room) was calculated following the equation:

$$q_e = \frac{(C_0 - C_e) \times V}{m} = \frac{(C_0 - C_e) \times 100}{0.2} \ldots\ldots\ldots\ldots \textit{eq.1}$$

Where, "C_0" and "C_e" are respectively the initial and the equilibrium concentration (ppm or mg L^{-1}), "V" is the total volume of solution (mL) and "m" is the amount of adsorbent used (g). The lamp was only turned on after 60 min of adsorption in the dark room. At the same time that the lamp lights up, the solution of methanol was added in the reactor which was kept under continuous visible irradiation at total time of reaction of 150 min. Uptakes of the solution were collected after each 10 min of test (using a syringe and a lid with 0.5 cm

diameter at top of the reactor to allow sampling based time). In order to limit the turbidity, membrane containing filters (0.2 μm of porosity) systematically used.

Using Shimadzu-UV-2501PC spectrophotometer, the UV-vis spectra permitted formaldehyde and Rhodamine-B quantifications in aqueous solution as a function of time (see §.4.1). Using the Beer-Lambert equation ($A=\varepsilon \times C \times L$), concentration was calculated with $C=A/19400$ equation in $mol.L^{-1}$. In reactivity part (see §.4.), the concentration in parts-per million (ppm) was used to monitor all evolution of the photocatalytic reaction, then, in water solution, the conversion of concentration in molarity ($mol.L^{-1}$) to concentration in ppm was calculated using equation: $C_{(ppm)}=[10^6 \times C_{(mol/L)} \times M_{(g/mol)}]/998.2071_{(kg.m-3)}$; where "M" is molar mass (479.02 $g.mol^{-1}$ for Rhodamine-B, 32.04 $g.mol^{-1}$ for methanol and 30.03 $g.mol^{-1}$ for formaldehyde) and 998.2071$kg.m^{-3}$ is the water solution density at temperature of 20ºC.

Commercial Rhodamine-B with its general formula $C_{28}H_{31}N_2O_3Cl$ and chemical name 9-(2-carboxyphenyl)-6-diethylamino-3-xanthenylidene]-diethylammonium chloride (noted RhB) was purchased from BIOCHEM (ChemopharmaAssay.97%). RhB is a fluorophore compound that belongs to the family of Xanthenes; this complex molecule contains an oxygen atom between two phenyl rings and some electronic properties easily detected by UV-visible spectroscopy. RhB is widely used because of its high fluorescence quantum yield and reported good photo-stability in water [45].

Formaldehyde was quantified by its absorption at 305 nm using UV-vis spectroscopy and 6 points calibration curves [46]. The photocatalytic transformation of methanol in formaldehyde in presence of RhB was described by a pseudo-first-order kinetic law according to the Langmuir-Hinshelwood model, so the rate of photocatalytic removal of RhB could be expressed by the following relationship:

$$C_t = C_0 \times e^{-k \times t} \ldots\ldots\ldots \textit{eq.2}$$

Where "C_t" represents RhB concentration at time "t" of irradiation, "C_o" is the initial concentration, "k" is the apparent reaction rate constant of the pseudo-first-order kinetics and "t" is irradiation exposure time [47]. Consequently, after many mathematical equations, the photo-removal efficiency (% of removal) of RhB was calculated using three steps [48]:

$$\frac{C_t}{C_0} = e^{-k \times t} \rightarrow \mathrm{Ln}\left(\frac{C_0}{C_t}\right) = k \times t \rightarrow \%\ \text{of removal} = \frac{C_0 - C_t}{C_0} \times 100 \ldots\ldots \textit{eq.3}$$

2.4. Spectroscopic detection of molecules alone:

For an organic molecule, three possible electronic transitions, as σ–σ*, π–π* (or π–σ*) and n–π*, are shown in our schematic representation of Fig.2-A. According to Mc Connell **[49],** the solvents, such as methanol, ethanol, n-hexane…etc, present absorptions with blue or red color according to the position of their different bands obtained in the visible domain of electromagnetic spectrum, Mc Connell [49] also mentioned electronic transitions in the UV region (< 400nm). The electronic transitions that we have schematized (Fig.2-A), result from the interaction of ultraviolet-visible radiations with an organic compound

containing atoms with hybridized atomic orbital, combinations s-p (as methanol and formaldehyde). The σ→σ* transition requires more energy and is not observed in the UV-vis range. Only π→π* and n→π* electronic transitions are detected in the UV-vis region in good agreement with [49].

Three spectra are depicted on Fig.2- B, C, D and were measured on: *(i)* aqueous solution containing 10 ppm of RhB dye (as in the conditions of our work) *(ii)* 0.25 ppm of methanol diluted in water and *(iii)* 30 ppm of formaldehyde diluted in water. The UV-vis spectrum of RhB dye (Fig.2-B) revealed an intense band centered at 554 nm accompanied by a second band (300-400 nm) of lower intensity, identified as an impurity of RhB commercial product. The UV-vis spectra of methanol and formaldehyde solutions are displayed in Fig.2-C and Fig.2-D. The nominal concentration of methanol was fixed to 0.25 ppm and experimental concentration was found as 0.2 ppm. Moreover, the nominal concentration for formaldehyde corresponded to 30 ppm against experimental concentration of 29 ppm. Given the close value between nominal and experimental concentrations, these experiments were conclusive to identify different spectroscopic bands of methanol and formaldehyde. Indeed; three electronic transitions were identified in Fig.2-C and attributed to π→σ* (λ_{max}:210 nm), π→π* (λ_{max}:280 nm) and n→π* (λ_{max}:512 nm) of methanol. For formaldehyde (Fig.2-D), only two clear electronic transitions are identified and attributed to n–π* (λ_{max}:305 nm) and π–π*(λ_{max}:230 nm) electronic transitions.

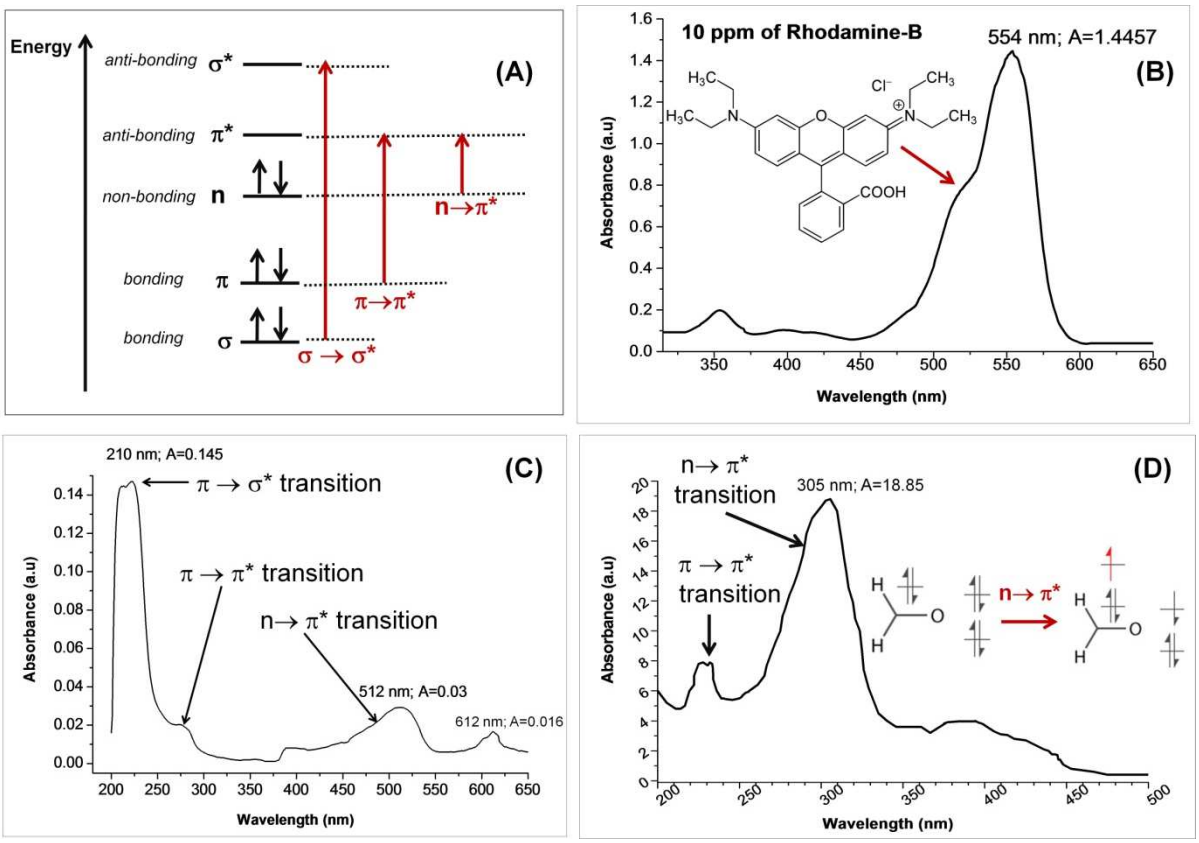

Figure-2. **(A)** Representation of different transitions under UV–vis light and the UV–vis spectra of aqueous solutions of: **(B)** 10 ppm of RhB, **(C)** 0.25 ppm of methanol and **(D)** 30 ppm of formaldehyde.

2.5. Physicochemical characterizations:

X-rays diffraction(XRD): the solid catalysts were analyzed by XRD and their patterns were recorded on a Bruker Advance D8 diffractometer using the Cu Kα radiation with steps of 2θ =0.02°, a count time of 6 s at each point and an X-ray power of 40 kV and 40 mA. The size d_p was calculated using the Debye–Scherrer formula, $d_p=(0.9\times\lambda)/(B\times\cos\theta)$, where λ is the X-ray source wavelength (λ_{cu}=0.15418 nm), B is the full-width at half maximum of the Bragg diffraction peak. A size of coherent domain (2θ=20-30°) was obtained by applying Debye–Scherrer equation on the (101) indexed peak of TiO_2 anatase. The measurement is valid in the direction perpendicular to the (101) plane. LeBail refinement was carried out using FullProf-2017 software [50]. The identification of phases was made by comparison with ICDD standard cards. Firstly, the positions of the peaks were corrected for zero-shift error by successive refinements, using detailed account of the mathematical procedures implemented in LeBail Fit. Secondly, considering the integrated peaks intensity of the refined function of structural parameters, the Marquardt least-squares procedure was adopted for minimizing the difference between the observed and simulated powder diffraction patterns. The progress of the minimization was monitored through the usual reliability parameters R_{wp} (weighted residual factor) and R_{exp} (expected residual factor) defined as follows [51]:

$$R_{wp} = \left(\frac{\sum_i wi\,(I_0-I_c)^2}{\sum_i Wi\,(I_0)^2}\right)^2 \ldots\ldots\ldots eq.4$$

$$R_{exp} = \left(\frac{N-P}{\sum_i Wi\,(I_0)^2}\right)^2 \ldots\ldots\ldots\ldots eq.5$$

Where "I_0" and "I_c" are respectively the experimental and the calculated intensities; $w_i=1/I_0$ (inverse of I_0) are weight factor and $w_i(I_0)$ is called the estimated standard deviation.

FEG/SEM and EDS: SEM images were acquired thanks to a FE-SEM Schottky gun SU-70 purchased from Hitachi (Japan). In order to prevent charging effect from the samples, low voltage (either 1 or 5 kV) conditions were used. Elemental atomic distribution in the near surface of samples was measured by EDS. The system used was on OXFORD X-Max 50mm^2 (SDD technology) spectrometer controlled through INCA software. The system was mounted on the FESEM Hitachi SU-70. To achieve a small volume analysis suited to the small particle size, 5 kV analyses were processed. Elemental standards samples fitted to these conditions were set up in a system (commercialized by Geller microanalytical laboratory, Boston, MA, USA). Quantifying correction model was Phi(phoz) model modified by Pouchou&Pichoir.

X-rays fluorescence (XRF): XRF spectra were measured with XEPOS (SpectroAmetek) spectrometer. With this apparatus, quantification of all elements with Z values 12<Z<92 is possible, so the oxygen is not quantified with the used equipment. The elements are quantified as milligrams per kilogram (ppm) or as atomic percentage.

N_2 sorption: the textural properties of the solids were determined by N_2 sorption data obtained at -196°C with an ASAP 2010 Micromeritics instrument or a Bell Instrument. Prior to the analysis, the samples were out gassed at 300°C for 3 h until a stable static vacuum of 0.263 Pa was reached. The weight of the sample used (initially around 80 mg) was measured

exactly after pretreatment. The BET (Brunauer Emmett Teller) specific surface area was calculated from the adsorption data over a relative pressure range from 0.05 to 0.30, as recommended for mesoporous solids [52]. The pore diameter and pore volume were determined according to the Barrett Joyner and Halenda (BJH) model applied to the desorption branch of the isotherm.

Diffuse reflectance UV-visible spectroscopy: spectra of solids were recorded at room temperature for 3-4 mm thick powder samples between 200 and 900 nm with a scanning rate of 200 $nm.min^{-1}$ on a Varian Cary 5000 spectrometer equipped with an integrating sphere of 70 mm diameter (Apparatus name: V-630-Instrument ; serial N°C390361148 ; Abs.Start: 900 nm ; Abs.End: 200 nm ; data interval= 1.0nm ; UV/Vis bandwidth=1.5nm ; light-source= D2/WI ; changing source at 340 nm and standard scan speed 400 $nm.min^{-1}$). The spectra were plotted in absorbance then reflectance modes, after subtraction of the Teflon reference PTFE signal. They were also used for estimation of "α", the absorption coefficient, equal to $[2.303\times\log(I_0/I)]/L$ with "L" corresponding to the path length taken here as 100 nm, "I_0" to the input light intensity and "I" the transmitted intensity.

2.6. Band gap calculations:

The optical properties enabled us to localize the electronic bands of support and two photocatalysts with respect to vacuum. For a comparison, band gap energy (E_g) was calculated by two methods: using either Kubelka-Munk function noted F(R) (not sensitive to direct or indirect electronic transition) and or Tauc's equation (applied for direct and indirect electronic transition). The F(R) Kubelka-Munk function (called K(S)), given as follows:

$F(R) = K/S = [(1-R)^2]/2\times R$……*eq.6*

Where R is the absolute diffuse reflectance for an infinitely think sample, "K" and "S" are respectively the sample absorption coefficient and scattering coefficient [53]. The energy of the band gap (E_g) value was determined for an indirect electronic transition by the slop of reflectance at maximum of wavelength of sample. The optical energy band gap was calculated using this relationship [54]:

$$Eg = \frac{h\times C}{\lambda} = \frac{1240}{\lambda}$$……..*eq.7*

Where "h" is the Planck's constant ($h=4.13510^{15}$eV.s), "C" is the light speed in vacuum (3.10^8 m/s) and "λ" (nm) is the wavelength. The Tauc's equation is written as follows:

$$\alpha\times h\times\nu = A\times\left(h\times\nu - E_g\right)^n$$……eq.8

It can be obtained:

$$(\alpha\times h\times\nu)^{\frac{1}{2}} = A\times\left(h\times\nu - E_g\right)$$

or

$$(\alpha\times h\times\nu)^2 = A\times\left(h\times\nu - E_g\right)$$

Where “A” is proportionality constant, “h” is the photon energy and “α” is the extinction coefficient. The value of “n” depends on the inter-band transition mechanism of materials. In eq.8, the n=2 value corresponds to first indirect allowed transition for TiO_2 according to the literature [55-56]. From two Tauc’s plots, the extrapolation of the intercept of the straight lines from $(\alpha h\nu)^2$ or $(\alpha h\nu)^{1/2}$ with the *x*-axis give respectively the direct band gap (corresponds to the charge transfer) and indirect permitted band.

3. Results and discussion.

3.1. Structure by XRD andLeBail refinement:

XRD patterns of Millennium-P500 (commercial) support, 3Zn/a-TiO_2 and 3Cu/a-TiO_2 catalysts are displayed in Fig.3. A single TiO_2 anatase phase was detected and corresponds to ICDD#021-1272. This single phase corresponds to a body-centered tetragonal lattice and to *I41/amd* space group. Lines of the Millennium-P500 sample are larger than the ones of calcined solids. As shown in Fig.3, calcined 3Cu/a-TiO_2 and 3Zn/a-TiO_2samples present similar diffraction peaks in 35-40°, 50-60° and 65-80° of 2θ domain but the absence of XRD-lines of CuO (ICDD#003-1018) and ZnO (ICDD#036-1431) phases can be noted. Indeed, it is known that is not possible by XRD technique to observe some phases with a percentage <5%wt.

For all samples, the ratio of R_{wp}/R_{exp} (by applying LeBail refinement) and the average crystallite sizes (calculated by Debye–Scherrer formula) and unit-cell parameters (estimated by LeBail refinement) are summarized in Table.1. It is known that quality of LeBail refinement is verified by two numerical statistical indicators R_{wp} and R_{exp} (eq.4 and eq.5 of §.2.5, using FullProf-2017 software). Here, with applying LeBail analysis, the true intensity of diffraction could be predicted and be the model obtained by minimizing the weighted sum of squared differences between observed and calculated intensities value. The R_{wp}/R_{exp} ratio (GoF=R_{wp}/R_{exp}: Goodness-of-Fit) varies in the following order: 3Zn/a-TiO_2 (2.75)> a-TiO_2 (2.2)> 3Cu/a-TiO_2 (1.74); it can be noticed that the GoF of 3Cu/a-TiO_2 is larger than the one measured on blank a-TiO_2, as can be expected because of the used calcination treatment and of the presence of nitrates salts in preparation steps. It is known that in a perfect refinement, the squared ratio R_{wp}^2/R_{exp}^2 should be less than 4 at the end of refinement. By comparing the results of calculation as shown in Table.1, for the measurements made on 3Cu/a-TiO_2 with “V12” with a corrected slot defined on the apparatus and with fixed slots, “FS” measurements have to be done under the two conditions but the non-coherent domain between the two files can be obtained with a SmartLab (high-resolution software). No noticeable difference was detected.

The sizes of titania particles were determined by XRD using Debye–Scherrer equation (analysis of full width at half maximum, FWHM) as shown in Table.1. Crystallites size (non-coherent domain sizes) were measured perpendicularly to the (101) indexed reticular plans that give the most intense diffraction peak and increase in the following order: Millennium-P500 (47.4 nm)<a-TiO_2 (118.6 nm)< 3Cu/a-TiO_2 (149.0 nm)< 3Zn/a-TiO_2 (223.0 nm). There is a high decrease in particle size after the impregnation step and the applied calcination

indicating an important sintering. The 3Zn/a-TiO_2 catalyst showed an increase of crystallites size more important than 3Cu/a-TiO_2.With the plans indexed (103) and using Scherrer expression, a size of 40.8 nm was measured for a-TiO_2 and 3Cu/a-TiO_2 against 61.2 nm for 3Zn/a-TiO_2. We have measured the particles sizes using the other diffraction peaks indexed 101, 200 and 204 and found significantly different values that are indicated in Table 1. The observed differences indicate anisotropic nanoparticles and the presence of anisotropic titania particles has been confirmed by FX and EDS characterizations (see further §.3.3).

From data of Table-1, the equality "a=b" and the almost constant value of "c" unit cell parameters indicated that neither Cu nor Zn species have penetrated inside the anatase titania lattice. Indeed, ionic radii of hexa-coordinated Cu^{+} or Cu^{2+}, Zn^{2+} and Ti^{4+} surrounded by oxygen species are significantly different and equal to 0.77, 0.73, 0.74 compared to 0.61Å. Penetration in lattice positions, reticular as well as interstitial yield to significant increase in unit-cell parameters [57] that we have not detected here.

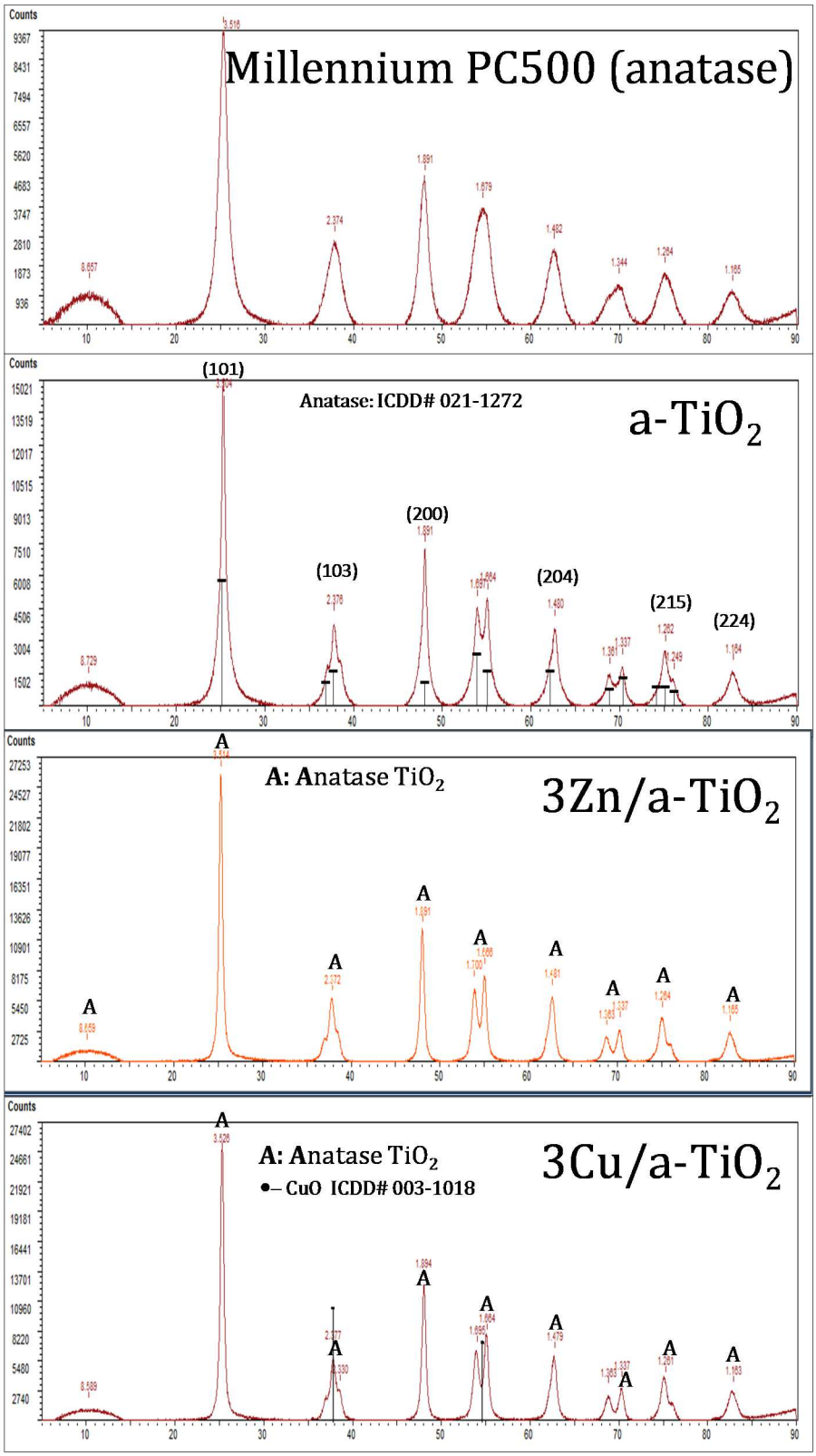

Figure-3. X-rays diffraction patterns of Millennium PC500, a-TiO_2 support and Zn and Cu-loaded catalysts.

Table-1. Unit-cell parameters of predominant anatase phase and average crystallite sizes corresponding to Millennium PC500, support and two catalysts. V12: mobile slots (XRD using Fit2D and V12.077-software); FS: Fixed slots (high-resolution diffractometer using fail-safe). The incertitude on crystallites size ≈ ±0.05.

Sample	R_{wp}*	R_{exp}*	R_{wp} /R_{exp}*	a=b ** (Å)	c * (Å)	Crystallites size for (101) plans (nm)	Crystallites size for (103) plans (nm)	Crystallites size for (200) plans (nm)	Crystallites size for (204) plans (nm)
Millennium PC500	/	/	/	/	/	47.4	30.6	50.2	33.9
a-TiO_2 (V12)	9.88	4.89	2.2	3.78	9.51	118.6	40.8	63.3	45.2
3Cu/ a-TiO_2 (FS)	14.00	7.70	1.81	3.78	9.51	/	/	/	/
3Cu/a-TiO_2 (V12)	7.52	4.30	1.74	3.78	9.51	149.0	40.8	126.6	67.7
3Zn/a-TiO_2 (V12)	11.20	4.07	2.75	3.78	9.50	223.0	61.2	126.6	67.7

:** calculations from LeBail refinement method (using FullProf-2017 informatic package); *:** body-centered tetragonal group I_4/amd group ($\alpha=\beta=\gamma=90°$; $a=b\neq c$)

3.2. Titania grains shapes and surface deposits by SEM and EDS:

The comparative study by FEG-SEM was conducted for the support and the Zn/Cu-loaded calcined catalysts to determine particles morphologies. On the three micrographs presented on left of Fig.4, random grains morphologies with lengths in the range of 500-1000 nm are observed. The support displays some agglomerations of grains on near-surface of 3Cu/TiO_2 and 3Zn/TiO_2. The selected grain (surrounded by circle on 3Zn/TiO_2 micrograph) presents a pseudo-spherical form with cross-section facets. Some small pseudo-spherical nanoparticles (in white color) are observed on the surface of grains and their identification requires EDX analysis (see further §.3.3)

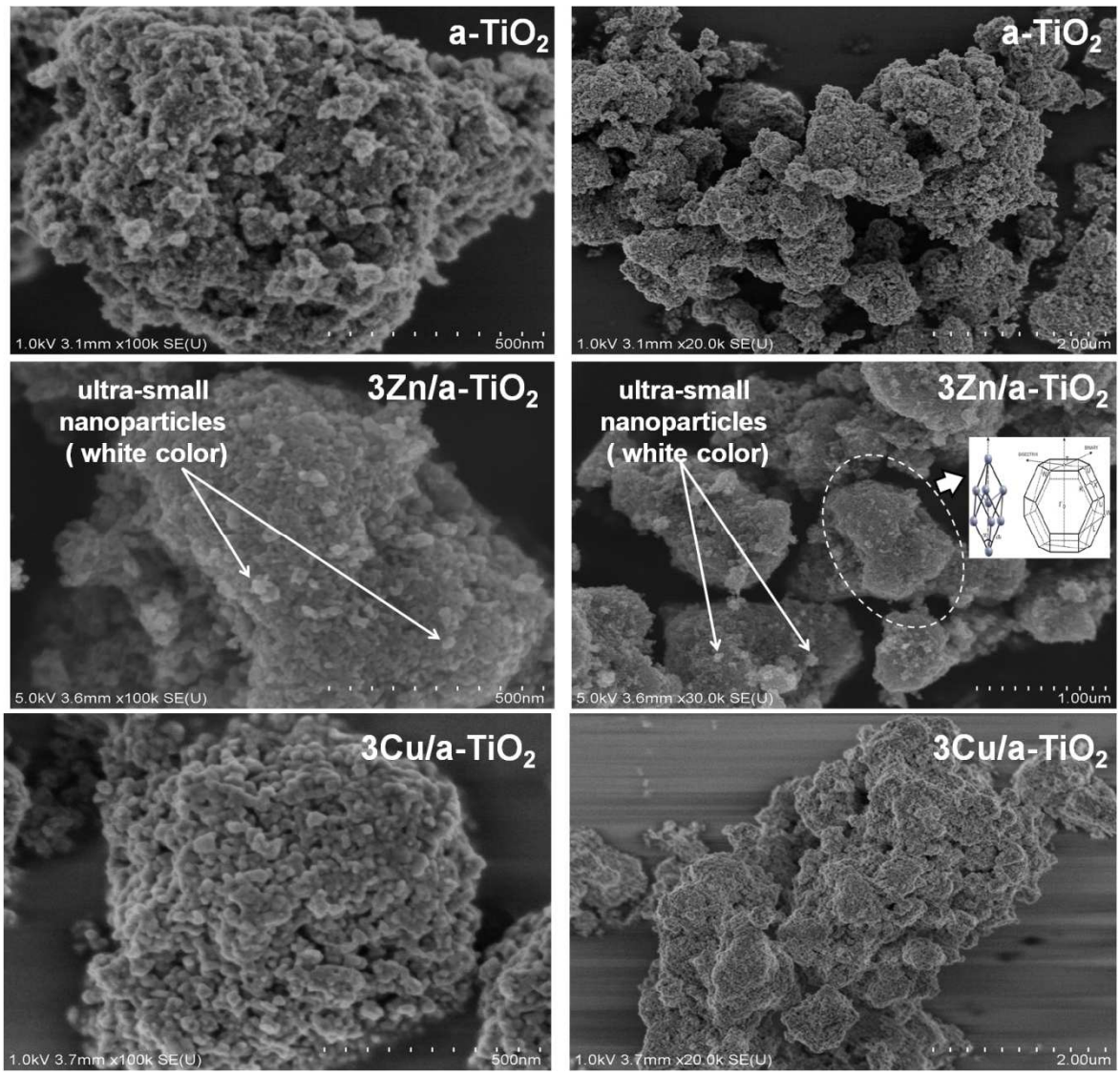

Figure-4. FEG-SEM**-**micrographs for two catalysts and support with: **(Left)** three enlargement images at scale=500 nm **(Right)** three images at : scale=2 µm (up), scale=1µm (center) and scale=2 µm (down).

3.3. Atomic composition by EDS and FX:

For 3Zn/a-TiO_2 and 3Cu/a-TiO_2 catalysts, Fig.5 shows the recorded FEG-SEM micrographs with their corresponding EDS spectra. Table 2 summarizes the atomic percentages obtained by the quantification of EDS peaks and the chemical compositions given by X-rays fluorescence (FX). In FEG-SEM mode, the electron beam was focused directly on Cu and Zn-containing nanoparticles to reveal their intimate composition (at 5 kV, with a probing in spherical volume of approximately 200 nm of diameter). Peaks are associated with electrons return to the K electron shell of O atoms and L shells of Ti, Zn and Cu atoms. On Fig.4, some traces of carbon were detected due to an air contamination (carbonates, CO_2) during the calcination step and air storage, furthermore, before EDS analysis, the samples

were out-gassed under vacuum, and despite this degassing step a percentage of carbon was detected probably due to some strong adsorption of this carbon in some surface depth.

EDS-spectra of two catalysts reveal different atomic percentages (Table 2), as more copper (2.46%) than zinc (1.33%) at the surface (these compositions are calculated in a volume of surface).The Zn/Ti and Cu/Ti atomic ratios (obtained by X-ray fluorescence) are close and indicated a similar distribution of Zn and Cu nanoparticles despite different radii of the two Cu and Zn elements. However, based on O/Ti atomic ratio (obtained by EDS), the surface of 3Cu/a-TiO_2 was observed to be richer in oxygen species than that of 3Zn/a-TiO_2 (78.87% against 61.2%); this last result is in good agreement with work of **[58]** which found same oxygen-enrichment in their study of characterizations of their nanopowders based on titanium dioxide TiO_2 modified with 1%(mol) of: copper, zinc and copper+zinc (with various Cu:Zn atomic ratios), prepared via a sol–gel route and thermally treated at 450°C. These authors explain that neither copper nor zinc entered into the TiO_2 structure (a point that was confirmed by XRD, like in the present study) but that oxides nucleated at the surface of titania particles, as probably in our case. In fig.5, the white dots sizes of copper or zinc (saved in files of the analysis) are circa 70 nm and then are too small to be detected by XRD.

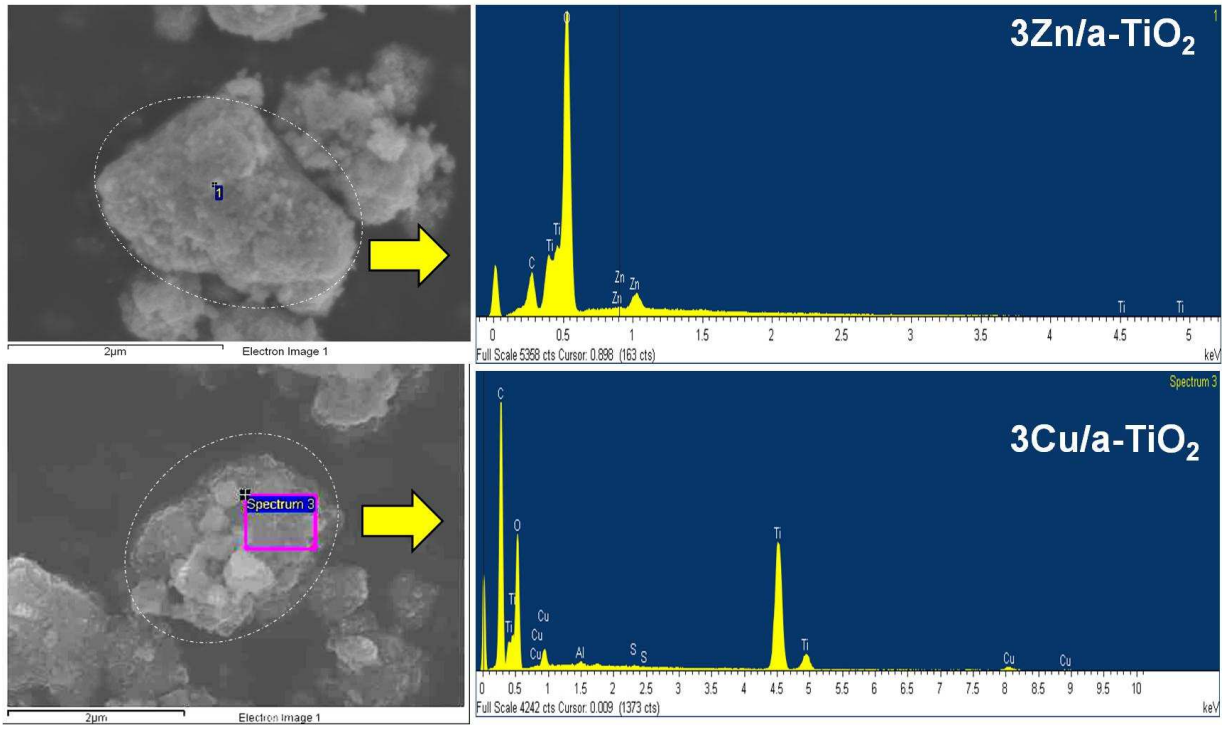

Figure-5. Typical SEM micrographs with EDS chemical analysis of two catalysts (the two circles targeting similar white areas).

Table-2. Quantification obtained by EDS and FX for two catalytic formulations of catalysts.

Catalysts	Grain dimension (μm) *	Atomic percentages (EDS) **	O/Ti (EDS)	Atomic ratios Zn/Ti and Cu/Ti (EDS)	Atomic percentage of Ti (FX)	Atomic percentage of Cu (FX)	Atomic percentage of Zn (FX)	Atomic ratios Zn/Ti and Cu/Ti (FX)
3Zn/a-TiO_2	2.06	Ti_L: 23.8 O_K: 61.2 Zn_L :1.3	2.57	0.04	53.70	/	2.91	0.054
3Cu/a-TiO_2	2.39	Ti_K: 18.7 O_K: 78.9 Cu_L: 2.5	4.22	0.13	56.16	2.67	/	0.047

*: indexed in Fig.4 (by white circle) and measured dimension using the ImageJ software package (1.52h, National Institutes of Health, Madison, WI, USA, 2018) ; **: spectra quantification from Fig.5 with the precision = ±0,1%wt.

3.4. Textural properties by N_2 sorption:

Nitrogen adsorption-desorption results are reported in Table.3. The commercial Millennium-PC500 sample was also studied by other authors [59]; they revealed a high BET surface (Table.3). As noted in comparison to a-TiO_2 support; Millennium-PC500 has a smaller specific surface due to the calcination (20% of mass loss); this decrease of S_{BET} could be related to pre-agglomerate of Millennium-PC500 grains in the step of preparation of a-TiO_2 associated to the increase of crystallites size (see XRD, §3.1.). Otherwise, S_{BET} of support is relatively small compared to those of 3wt% Cu, Zn catalysts, this surface increased in the following order: a-TiO_2(50.1 $m^2.g^{-1}$)<3Zn/a-TiO_2 (80.0 $m^2.g^{-1}$)<3Cu/a-TiO_2(84.4 $m^2.g^{-1}$). This increase of BET-surface occurred after the impregnation process and calcination step and might be related to the presence of Cu and Zn oxide nanoparticles at the catalytic surface. This result is consistent with our XRD findings (Table.1), which showed the increase of all crystallites sizes after the impregnation process related to the Cu and Zn nanoparticles insertion in surface-layer of a-TiO_2 support. Previous papers [60] reported that when a metal is incorporated into the pores of support, the surface area decreases due to the partial pore blocking, but in our case, the oxide species are attached to the support surface and not incorporated in the pores of a-TiO_2 support or in the support itself. Note that pores volume (Vp) remains constant after the impregnation process.

Table-3. Textural characteristics of all samples (BET-surface, porous volume and average pore).

Samples	S_{BET} ($m^2.g^{-1}$)	V_p($cm^2.g^{-1}$)	"d_p" Average pore diameter (nm)
MillenniumPC500 (≥99% anatase)*	287	/	5–10
a-TiO_2	50.1	0.24	13.2
3Zn/ a-TiO_2	80.0	0.21	10.7
3Cu/ a-TiO_2	84.4	0.21	10.2

*: Reference [59]

3.5. Optical properties by UV-visible spectroscopy:

In order to compare the band gap value (noted Eg), Kubelka-Munk and Tauc direct and indirect transitions (see equations of §.2.6) were used for the computation. The results from UV-visible investigation (reflectance spectra and band gap calculations) on the catalysts and support are plotted in Fig.6**.** As displayed in the reflectance spectrum of a-TiO_2, a first (d-d) intra-metallic peak of absorption (Fig.6-on top) is observed, implying that Ti^{3+} ions are present (with electronic configuration [Ar]$3d^0$).This wide signal is located in the visible region with an extension to near infra-red region above 800 nm. Always for this sample (a-TiO_2 thermally activated), a band between 500 and 1000 nm is attributed to Ti^{3+} ions surrounded by 6 oxygen ligands (as in $Ti(OH)_6^{3-}$ clusters). Unfortunately, it is not possible to distinguish the O-atoms of a water molecule from an OH or an oxygen-atom of the titania surface, all these atoms having the same spin-orbit constant [61-63]. Mac Donald et al. [59] have characterized the commercial Millennium-PC500 by EPR spectroscopy and observed interstitial Ti^{3+} signal inside the bulk of anatase crystals. These cations cannot be located on titania surface because if they were located on the sample surface, an important signal broadening would be observed because of dipolar couplings with paramagnetic O_2 molecules.

With 3Cu/a-TiO_2 sample, the signal due to Ti^{3+} ions was also observed and associated with a second absorption that corresponds to another d-d intra-metallic electronic transition inside Cu^{2+}cations surrounded by 6 oxygen ligands, forming an octahedral crystal field. Indeed, these cations with electronic configuration "[Ar]$3d^9$" can be attributed to $(t_{2g})^6(e_g)^3$ repartition of electrons on the five "d" orbitals. The last 3d atomic orbital is the $3d_z^2$ and the observed transition corresponds to the promotion of electrons from the $3d_{x^2-y^2}$ orbital to this partially occupied $3d_z^2$ orbital. This transition is associated with a broad absorption, with a maximum value located circa 800 nm.

For 3Zn/a-TiO_2 sample, no (d-d) transitions were observed. This can be explained in part by the fact that Zn^{2+}cations have a complete electronic configuration [Ar]$3d^{10}$ but they cannot give electronic transitions. The absence of any signal due to Ti^{3+} ions is more surprising, but another band observed at 1400 nm, can be attributed to a transition between two metallic sites (e.g. Zn^{2+} and Ti^{3+}) or to existing Zn-O-Ti bonds in agreement with literature [64-65].

From Tauc and Kubelka-Munk curves (Fig.6), the intercept of the tangents with x-axis permits to determine the E_g band gap values. The plots relative to Tauc curves drawn for direct and indirect semi-conducting oxide represent respectively $(F(R)*E)^2$ and $(F(R)*E)^{1/2}$. The extrapolation of the straight line gives a direct band gap of 3.40 eV for support against 3.45 and 3.41 eV for respectively Zn and Cu containing catalysts. For all samples, the permitted indirectly transitions are observed at 3.10 eV. A small difference is observed between the results of the two calculation methods (Tauc and Kubelka-Munk).Whatever the used method, E_g values vary in the order: $E_g(3Cu/a\text{-}TiO_2)<E_g(a\text{-}TiO_2)<E_g(3Zn/a\text{-}TiO_2)$. It is important to know that for titania containing sample, density of state calculations are available in literature (DFT: Density functional theory calculations) and were found to be in excellent agreement with experimental [66], these calculations have shown that valence band of titania is mainly composed by O2p states and the conduction band by Ti3d states. The highest E_g of Zn-catalyst (3.45 or 3.46 eV) is related to the presence of better dispersion of Zn^{2+} oxide/hydroxide nanoparticles at the surface of titania, which create a molecular orbital located under the titania conduction band. Since Zn^{2+} cations have completely filled $3d^{10}$ electronic configuration, the observed electronic transition that is observed in that case is due to an electronic transition between the energy level of located Zn^{2+}cations and the conduction band of titania, important since it gives mobile electrons. These O-vacancies are associated with two electrons and give Ti^{3+} ions, preferentially located close to the incorporated larger Zn^{2+} cations. The energy of these Ti^{3+} sites is expected to be located just below the conduction band of titania. Even if Cu and Zn containing TiO_2 involve defects which by themselves can activate the photocatalytic properties of titania, the coupling between the new energy level under the conduction band of titania and the second energy level located above the valence band of titania can yield to a decrease of the photocatalytic properties of titania because of an unexpected electron transfer. According to the literature [67], a similar direct interplay has been observed between N-dopants (above valence band) and O-vacancies associated with Ti^{3+} ions (above conduction band): Ti^{3+}cations were not-detected because they provide one electron to the new energy level associated with N-dopants replacing O-atoms inside the titania bulk.

As conclusion, the $3Cu/a\text{-}TiO_2$ catalyst that we have prepared is strongly sensitive to visible light and contains like activated $a\text{-}TiO_2$ some Ti^{3+} ions. By contrast, Ti^{3+} ions are not detected in $3Zn/a\text{-}TiO_2$, an observation that we associate with the parallel formation of O-vacancies. These points give an indication in advance about the nature and domain of activity in photocatalysis which are then introduced. $3Cu/a\text{-}TiO_2$ is colored and will interact easily with visible light, while, $3Zn/a\text{-}TiO_2$catalyst is white and they will therefore allow less visible light absorption.

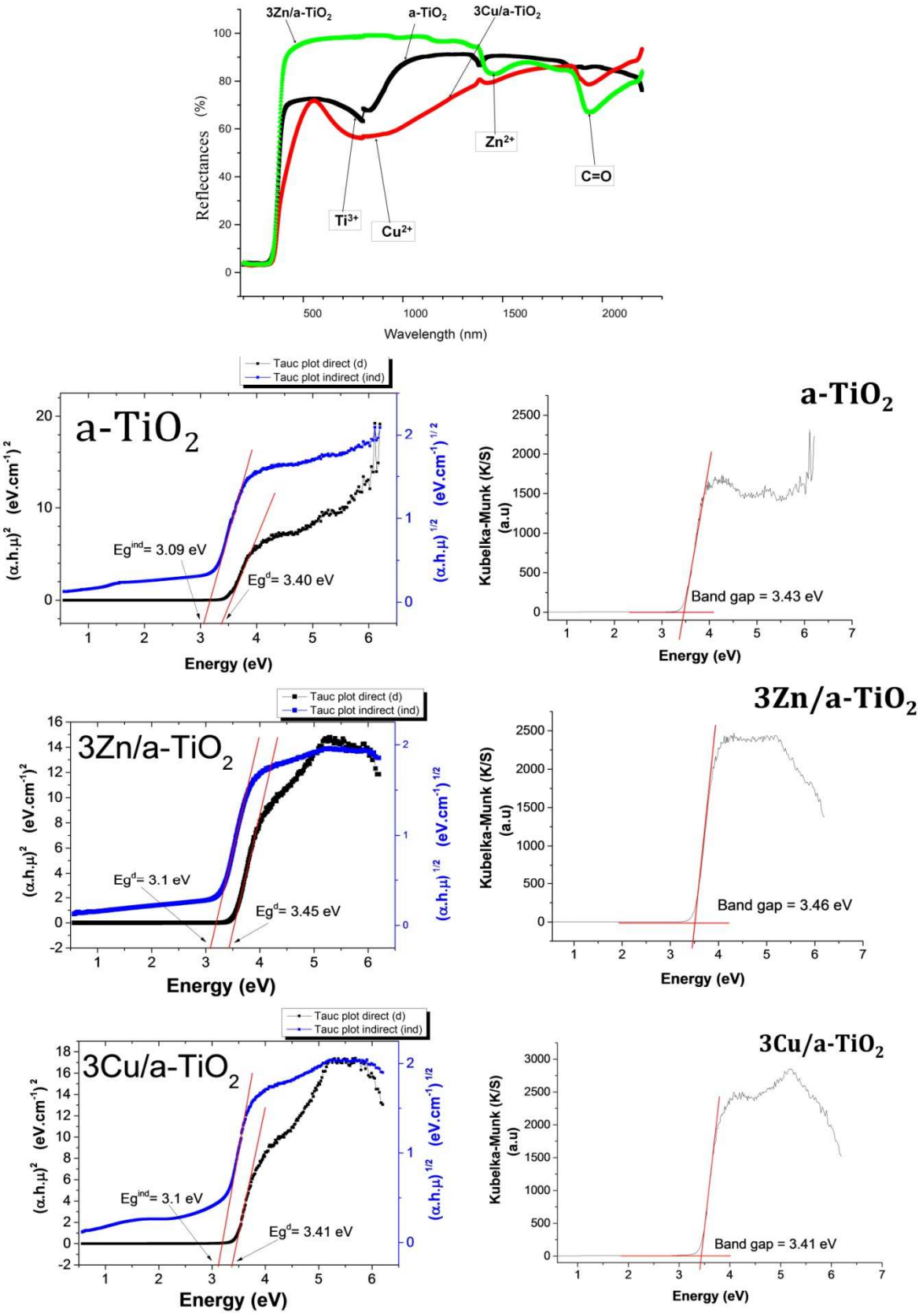

Figure-6. **<u>On top</u>:** UV-visible reflectance spectra versus wavelengths. **<u>Down:</u>** determination of optical transitions of support, zinc and copper samples by: *(Right)* Kubelka-Munk, *(Left)* Tauc plot direct and indirect transition.

4. Study of reactivity:

The photocatalytic performances of Millennium-PC500, a-TiO_2 (support), 3Zn/a-TiO_2 and 3Cu/a-TiO_2 catalysts were examined in dark and visible-light conditions. In dark conditions, the adsorption of 10 ppm of RhB aqueous solution (V=100 mL, pH=4.11) was performed to achieve an adsorption equilibrium during a time of 60 min. After this time, 100 mL of pure methanol was added to RhB solution and the visible irradiation is triggered. The concentration of methanol in the total volume (200 mL) was 3.37 ppm. The activity in the photocatalytic partial oxidation of methanol in presence of RhB dye (used as sensibilizer) was tested to produce formaldehyde in conditions mentioned above (see §2.3).

4.1. Photocatalytic activities of catalysts:

To study the role of catalyst in photocatalytic reaction under visible light irradiation, the efficiency of photo-oxidation of methanol was studied by Rhodamine-B and without catalyst. The results are presented in Fig.7-A and Fig.7-B. The reaction achieved without catalyst but gave very low yield of formaldehyde. Rhodamine-B degradation occured in the presence of two catalysts and of the support. For Millennium-PC500, a-TiO_2 (support), 3Zn/a-TiO_2 and 3Cu/a-TiO_2 catalysts, the Fig.7-C also shows the evolution of UV−vis spectra of RhB and formaldehyde during the photo-oxidation of methanol (0-150 min).

In Fig.7-A, in the absence of catalyst, the main band of methanol was observed which is due certainly to the absence of adsorption on the catalytic surface. On the other hand, the absence of Rhodamine-B the irradiation under visible light of methanol/Zn-catalyst did not led to the formation of formaldehyde (Fig. 7-B), which shows the role of RhB-dye as photo-sensibilizer in this photocatalytic reaction.

In Fig.7-C, it can be seen that except a secondary band of methanol centered at 620 nm, the main band of methanol (see Fig.2-C) was not observed in all spectra; therefore, the methanol cannot be quantified. The bands of formaldehyde (Fig.7-C) were observed at position circa 301 nm (according Fig.2.D). For 3Zn/a-TiO_2 and 3Cu/a-TiO_2 catalysts, the maximal wavelength for RhB (Fig.7-C) is constant and centered at 554 nm (according to wavelength positions of Fig.2-B in absence of any catalyst). In contrast, for Millenium-PC500 and a-TiO_2, a shift of its position over time was observed, certainly indicating a spontaneous and partial transformation of RhB in other derivative product. Indeed, Al-Kahtani [68] has reported that RhB ($C_{28}H_{31}N_2O_3Cl$) is degraded in several cyclic products by a partial oxidation (N-deethylation without cleavage of this dye) or degraded by a total oxidation (mineralization step) and has proposed a schematic mechanism corresponding to the following degradation:

Partial degradation:

RhB $\rightarrow$products (N-deethylation)$\rightarrow CH_2(OH)$-$CH(OH)$-$CH_2(OH)$+ products(cleavage)

The presence of intermediates of RhB obtained by deethylation is ascertained by the UV visible spectra presented in Figure 7. Here, we assume that their role on the activation of titania cannot be neglected.

Total degradation:

RhB$\rightarrow$(N-deethylation)$\rightarrow$(cleavage)$\rightarrow CO_2+H_2O+NO_3^-+NH_4^++Cl^-$(mineralization)

In a previous work [64], each reaction of deethylation was associated with a hypsochromic shift of the maximum attributed to RhB by 15 nm (at pH=4.7 and 10 ppm of Rhodamine-B+120 mL of water). This is consistent with the main shift observed here, due to single deethylation. With Millenium PC500 and a-TiO_2 samples, RhB neutral was partially preserved.

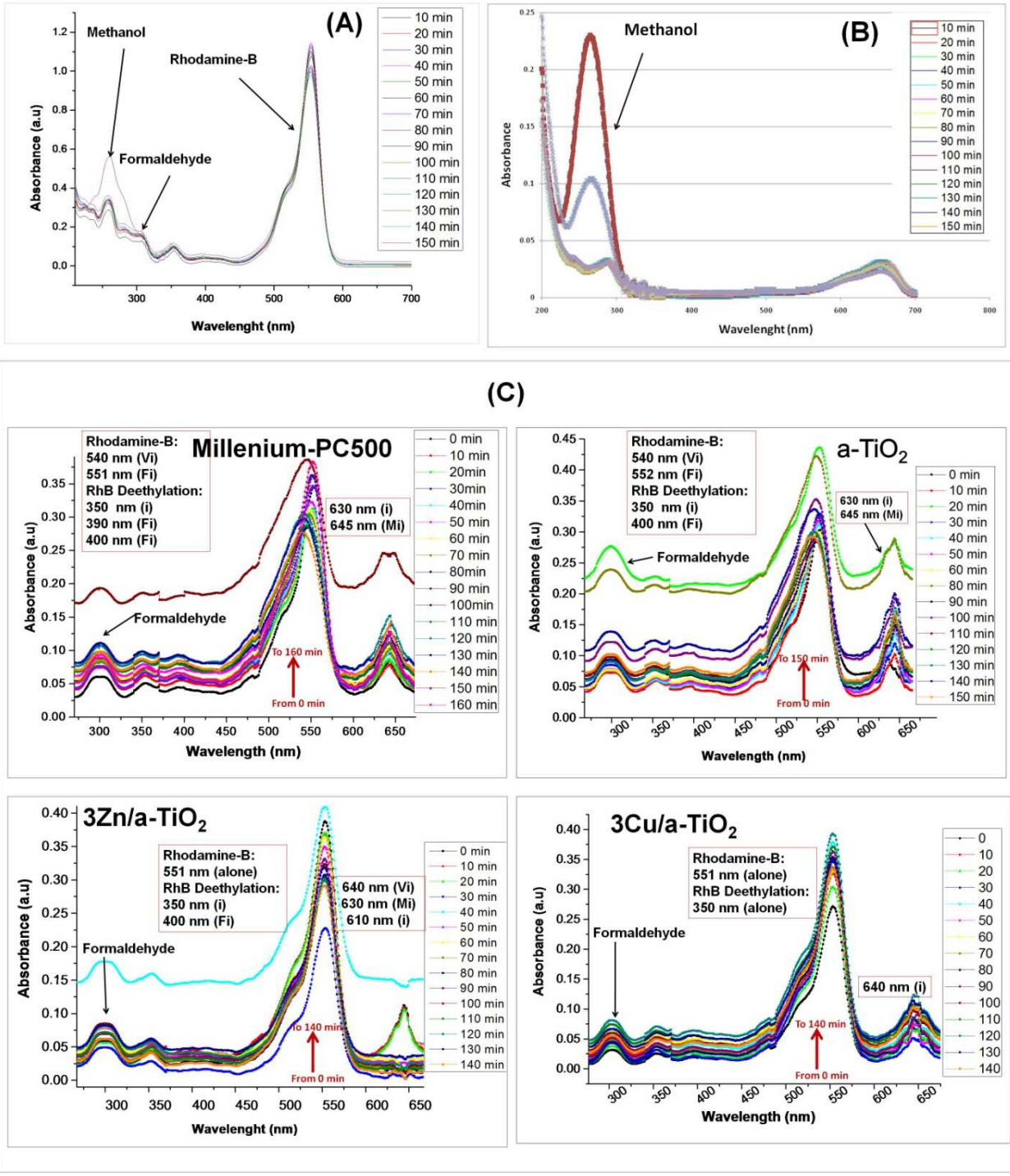

Figure-7. **(A)** Photocatalytic oxidation of methanol assisted by RhB without catalyst, **(B)** Photocatalytic oxidation of methanol with Zn-catalyst and in absence of RhB, **(C)** UV–vis spectra evidenced RhB photodegradation and formaldehyde formation with all samples and at different times of reaction (Vi:very intense, Mi: moderately intense, i: intense, Fi: few intense).

Under experimental conditions (catalyst mass: 200 mg, total volume: 200 mL, halogen lamp), the photocatalytic activity evolution was investigated by UV-vis spectroscopy in Fig.8. The variation of photo-removal percentage of RhB as a function of reaction time shows that copper catalyst led to a faster degradation of RhB than for the support and zinc catalyst. The improved performances of 3Cu/a-TiO_2 catalyst can be ascribed to the formation

of a particular hetero-structure between Cu(II) nanoparticles and a-TiO_2 support which may retard the recombination of photo-excited charge carriers.

The studies of RhB degradation after 20 min and 150 min of illumination and the adsorptive capacity under dark conditions are reported in Table-4. Compared to other samples, Millennium-PC500 reaches 30.4% after 150 min of visible light exposition and thereby was the least active sample. After 20 min of illumination, the percentage of RhB that have reacted (by partial deethylation or by decomposition) reached 87.8%(3Cu/a-TiO_2)>86.9%(3Zn/a-TiO_2)>68.6%(a-TiO_2)>9.5%(Millennium-PC500). An anomaly can been observed in the behaviors of copper and zinc catalysts after 50 min upon the visible light irradiation ; the first possible explanation is related to a possible decrease of the number of absorbed photons (h), the concentration of RhB increases because the path length of the generated photons in the solution decreases and the second explanation is a possibility of desorption of a number of RhB molecules already adsorbed on the catalysts, under the effect of excitation by continuous light. In dark conditions, the copper catalyst showed the highest value of adsorptive capacity of RhB molecules (14.51 $mg.g^{-1}$). The degradation of RhB at 60 min of visible light illumination was seven times higher compared to 60 min of adsorption in dark.

Over time of photocatalytic reaction, the removal of RhB dye from the aqueous solution was clearly observed, demonstrating that a surface-reaction between solid catalyst and RhB dye occurred. It is possible that; upon the visible light excitation, RhB molecules are excited with an electron in their lowest unoccupied molecular orbital and RhB molecules then act as electron donors to give $RhB^{+\bullet}$ radicals which structure is presented in Fig.2.B and these electrons (e^-) will further help in the transformation of methanol into formaldehyde. The progressive photo-degradation of adsorbed RhB sensibilizer was expected if "h^+" holes were not accessible inside the titania valence band. For Cu catalyst (with the smallest BG value and the highest photocatalytic activity), the removal of RhB from aqueous solution gives an indication about photocatalytic activity by RhB involvement in the transformation of methanol in formaldehyde. It is possible that e^- of the LUMO are transferred into conduction band of titania to give H_2O_2 molecules which further participate to the transformation of methanol to formaldehyde, in good agreement with mechanism of H_2O_2 formation (during photocatalytic reaction) mentioned in literature [69, 70]. The holes in valence band highly reactive species react with methanol to form stable methoxide groups with visible halogen lamp. The observed photocatalytic behavior depends on specific surface (S_{BET}: 50.1 $m^2.g^{-1}$ (a-TiO_2)<80.0 $m^2.g^{-1}$ (3Zn/a-TiO_2)<84.4 $m^2.g^{-1}$ (3Cu/a-TiO_2), following the same trend than the photocatalytic RhB-degradation, see above) and thus depends on the rate of the transformation of methanol to formaldehyde. It can also note that, the minimum band gap (E_g(3Cu/a-TiO_2)<E_g(a-TiO_2)<E_g(3Zn/a-TiO_2)) was found for the best active catalyst in the photocatalytic RhB-degradation. The photocatalytic results (97.7% of RhB-degradation for 3Cu/a-TiO_2 against 74.3% for 3Zn/a-TiO_2 at 150 min) could also depend on the amount of surface oxygen atoms, as we have observed more oxygen species by EDS for 3Cu/a-TiO_2 (78.9%O_K) than for 3Zn/a-TiO_2 (61.2%O_K); indeed, some authors [71] demonstrated through their proposed photocatalysis mechanism, that when the reactive oxygen species were more important at the interface of a catalyst, a higher capture of electrons by these species was

possible given the oxygen-sites number, and therefore could facilitate efficiently the photodegradation of the reactive molecule.

Adsorption capacity and photocatalytic properties for the removal of non-modified RhB (visible signal at 544 nm) are summarized in Table 4. According to the results of this table and spectra of Fig.7, the intermediates given by RhB at one, two, three or four deethylations are not introduced. The most represented intermediate (Fig.7) is the mono-deethylated radical. The 3Cu/a-TiO_2 catalyst, in which more absorption was detected, was also the most active one in the RhB-degradation photocatalytic reaction (Table-4).

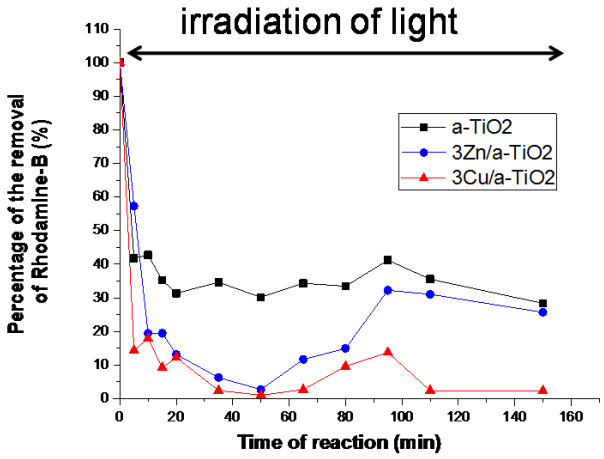

Figure-8. Photo-degradation of RhB in the visible-light photo-oxidation of methanol promoted by Cu and Zn catalysts and support.

Table-4. Adsorptive capacity (in dark conditions) and % of removal of non-modified RhB ($\lambda_{.Max}$=554 nm) during photocatalytic reaction (radicals formed by decomposition of RhB are very stables).

Catalyst	**Millennium-PC500**	**a-TiO_2**	**3Zn/a-TiO_2**	**3Cu/a-TiO_2**
"q_e" adsorptive capacity of Rhodamine-B (mg/g)*	13.6	14.11	13.07	14.51
Percentage of removal of Rhodamine-B (%) **	9.5	68.6	86.9	87.8
Percentage of removal of Rhodamine-B (%) ***	30.4	71.5	74.3	97.7

*: During 60 min of dark conditions; **: At 20 min of reaction; ***: At 150 min of reaction.

4.2. Productivity in formaldehyde:

The formaldehyde bands of samples are identified at wavelength centered at 301 nm and attributed to n→ π* electronic transitions (according Fig.2-D). The formaldehyde productivities (%) and CH_2O concentrations (ppm) recorded at 2h of photocatalytic reaction

were correlated to the crystallites size of (101) plans (XRD most intense peaks) and the investigated results are depicted in Fig.9. Productivity in formaldehyde was calculated using followed equation: $\%P = \frac{C_{formaldehyde}}{C_{methanol}} \times 100$; where "$C_{methanol}$" are the concentrations of methanol (ppm) introduced in the photocatalytic reactor and "$C_{formaldehyde}$" are the concentrations of formaldehyde (ppm) obtained by sampling analyzed by UV-vis spectroscopy (for a concentration of methanol of 3.37 ppm).

From Fig.9, a-TiO_2 and Millennium-PC500 appear more sensitive to the formation of formaldehyde alone whereas, crystallites with sizes >130nm and containing Cu or Zn-species (3Cu/a-TiO_2 and 3Zn/a-TiO_2) follow another reaction mechanism. The formaldehyde productivity varies in order: a-TiO_2(6.2%)>Millennium-PC500(4.9%)>3Zn/a-TiO_2(3.8%)≈3Cu/a-TiO_2(3.7%); the concentrations and productivities of the two metal containing catalysts are close but lower than the one of the supports, used as precursors. These differences are consistent with best oxidation properties observed with metallic species allowing better oxidation properties with 3Cu-TiO_2 and 3Zn-TiO_2 because formaldehyde is further oxidized to give formic acid and/or CO_2.

Indeed, the copper and zinc catalysts gave less formaldehyde amounts than the support but revealed the best activities. We suggest that in two catalysts, Cu and Zn elements are dispersed in the first layers of the surface (as shown by EDS and FX, in the form of nanoparticles of Cu or Zn oxides or hydroxides, which favored the mechanism of photo-oxidation and photo-dehydrogenation of methanol to formaldehyde and CO_2 (according $CH_3OH \rightarrow CHO \rightarrow CO_2$) which is this could explain higher activities, while support and Millennium-PC500 have led only to photo-dehydrogenation of methanol (according $CH_3OH \rightarrow CHO$).

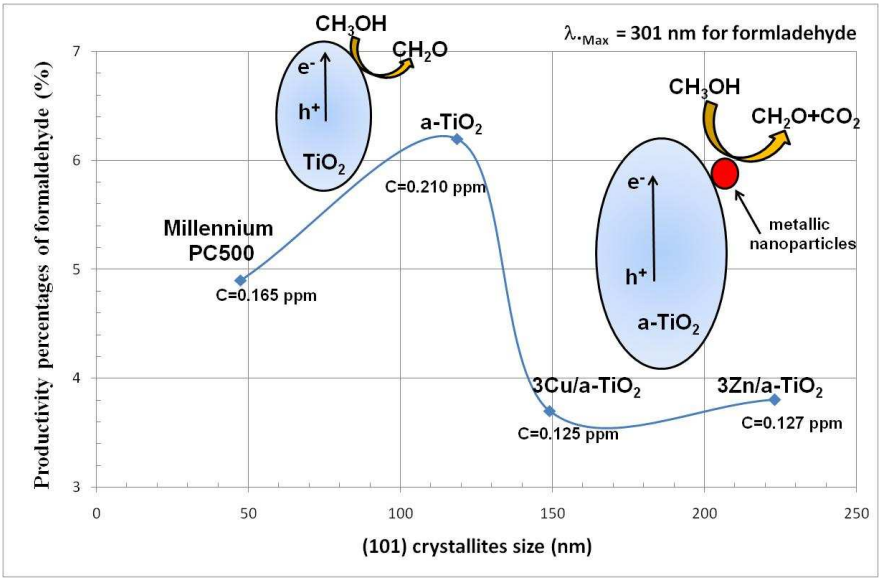

Figure-9. Concentrations (C) and productivity of formaldehyde (%) calculated from CH_2O-absorbance values ($\lambda_{.Max}$=301nm, molar mass=30.03 g.mol^{-1}) and obtained after 2.5h (or 150 min) of photocatalytic reaction.

An interest was brought to the photo-induced electronic transfer between nanoparticles of semiconducting oxides and a support such as titania, which is also a semi-conductor. We can

conclude that the electrons from Rhodamine-B are transferred into the conduction band of titania and participate to methanol oxidation for the production of formaldehyde. In our experimental conditions, we have observed by XRD that no penetration of Zn and Cu species inside titania (bulk) has taken place.

5. Conclusion.

We have shown in the present work that methanol in aqueous solution is oxidized to formaldehyde and other secondary products using a visible light excitation source and in the presence of Cu and Zn oxide or hydroxide nanoparticles dispersed on anatase (a-TiO_2) surface and Rhodamine-B dye as photosensibilizer. The 3Cu/a-TiO_2 and 3Zn/a-TiO_2 (with 3%wt in Cu or Zn) were found to give best formaldehyde yield with respect to other Cu or Zn contents studied in parallel work. Photocatalytic transformation of Rhodamine-B to a stable mono deethylated radical act to protect titania holes, necessary to activate the photo-oxidation of methanol. The photocatalytic removal of Rhodamine-B after 150 min of visible irradiation (Table-4) reached 97.7% for 3Cu/a-TiO_2, compared to 74.3% and 71.5% with respectively 3Zn/a-TiO_2 and a-TiO_2.

We have observed by UV-vis spectroscopy analysis in the 500-1000 nm range for Cu/a-TiO_2 a band assigned to Cu^{2+} corresponding to a d-d intra-metallic transition of Cu^{2+} ions in an octahedral crystal field and to an electronic repartition of $(t_{2g})^6(e_g)^3$ on 05 d-orbitals. It can be assigned to Cu oxide or hydroxide nanoparticles not detectable by XRD and deposited as a thin layer on TiO_2 surface. The E_g values were determined and observed to be E_g(3Cu/a-TiO_2)<E_g(a-TiO_2)<E_g(3Zn/a-TiO_2). The minimum band gap was found for the best active catalyst in the photocatalytic RhB-degradation, it is suggested that the best catalysts correspond to a strong connection between $Cu^{2+}$and Ti^{3+} cations.

The EDS technique allowed the detection of copper and zinc on TiO_2 particles, thus indicating a dispersion of the cations in the upper layers of TiO_2 surface and not into the bulk. EDS also reveals that 3Cu/a-TiO_2 (with 78.9%O_K) possesses a richer surface in oxygen compared to 3Zn/a-TiO_2 (with 61.2%O_K), which could also be related to the best activity of 3Cu/a-TiO_2.

Acknowledgements.

This work was supported by with funding from the Algerian Ministry of Higher Education and Research for Cooperation Program between LRS laboratory (UMPC Paris, France) and two Laboratories of Algeria. We also thank "Institut des Matériaux de Paris Centre (IMPC FR2482)" for funding of FEG-SEM & EDS characterizations.

References.

[1] M. Miyauchi, H. Irie, M. Liu, X. Qiu, H. Yu, K. Sunada, K. Hashimoto, Visible-Light-Sensitive Photocatalysts: Nanocluster-Grafted Titanium Dioxide for Indoor Environmental Remediation, J. Phys. Chem. Lett. 7 (2016) 75–84. doi:10.1021/acs.jpclett.5b02041.

[2] T. Wu, G. Liu, J. Zhao, H. Hidaka, N. Serpone, Photoassisted Degradation of Dye Pollutants. V. Self-Photosensitized Oxidative Transformation of Rhodamine B under Visible Light Irradiation in Aqueous TiO_2 Dispersions, J. Phys. Chem. B. 102 (1998) 5845–5851. doi:10.1021/jp980922c.

[3] L. Muszkat, L. Feigelson, L. Bir, K. a. Muszkat, Photocatalytic degradation of pesticides and bio-molecules in water, J.Pest Manag. Sci. 58 (2002) 1143–1148. doi:10.1002/ps.578.

[4] Y. Park, Y. Na, D. Pradhan, B.K. Min, Y. Sohn, Adsorption and UV/Visible photocatalytic performance of BiOI for methyl orange, Rhodamine B and methylene blue: Ag and Ti-loading effects, Cryst. Eng. Comm. 16 (2014) 3155–3167. doi:10.1039/c3ce42654h.

[5] S.A. Ansari, M.M. Khan, M.O. Ansari, M.H. Cho, Nitrogen-doped titanium dioxide (N-doped TiO_2) for visible light photocatalysis, New J. Chem. 40 (2016) 3000–3009. doi:10.1039/c5nj03478g.

[6] J.M. Chem, Recent advances in dye-sensitized semiconductor systems for photocatalytic hydrogen production, J. Mater. Chem. A Mater. Energy Sustain. 4 (2016) 2365–2402. doi:10.1039/C5TA08939E.

[7] E. Yoshioka, S. Kohtani, T. Jichu, T. Fukazawa, T. Nagai, A. Kawashima, Y. Takemoto, H. Miyabe, Aqueous-Medium Carbon − Carbon Bond-Forming Radical Reactions Catalyzed by Excited Rhodamine B as a Metal-Free Organic Dye under Visible Light Irradiation, J. Org. Chem. 81 (2016) 7217−7229. doi:10.1021/acs.joc.6b01102.

[8] M.Yin, Z.Li, J.Kou, Z. Zou, Mechanism Investigation of Visible Light-Induced Degradation in a Heterogeneous TiO_2/Eosin Y/Rhodamine B System, J. Environ. Sci. Technol. 43 (2009) 8361–8366. doi:10.1021/es902011h.

[9] Y. Bu, Z. Chen, Effect of oxygen-doped C3N4on the separation capability of the photoinduced electron-hole pairs generated by O-C_3N_4@$TiO_2$with quasi-shell-core nanostructure, J. Electrochim. Acta. 144 (2014) e42–e49. doi:10.1016/j.electacta.2014.08.095.

[10] J. He, J. Wang, Y. Chen, J. Zhang, D. Duan, Y. Wang, Z. Yan, A dye-sensitized Pt@UiO-66(Zr) metal-organic framework for visible-light photocatalytic hydrogen production, J. Chem. Commun. 50 (2014) 7063–7066. doi:10.1039/c4cc01086h.

[11] A. Ajmal, I. Majeed, R.N. Malik, M. Iqbal, M.A. Nadeem, I. Hussain, S. Yousuf, G. Mustafa, M.I. Zafar, M.A. Nadeem, Photocatalytic degradation of textile dyes on Cu_2O-CuO/TiO_2 anatase powders, J. environ.chemi.eng. 4 (2016) 2138-2146. doi:10.1016/j.jece.2016.03.041.

[12] Z. Li, A. Ivanenko, X. Meng, Z. Zhang, Photocatalytic oxidation of methanol to formaldehyde on bismuth-based semiconductors, J. Hazard. Mater. 380 (2019) 120822. doi:10.1016/j.jhazmat.2019.120822.

[13] A.C. Lausche, J.S. Hummelshøj, F. Abild-pedersen, F. Studt, J.K. Nørskov, Application of a new informatics tool in heterogeneous catalysis : Analysis of methanol dehydrogenation on transition metal catalysts for the production of anhydrous formaldehyde, J. Catal. 291 (2012) 133–137. doi:10.1016/j.jcat.2012.04.017.

[14] L.E. Heim, H. Konnerth, M.H.G. Prechtl, Future perspectives for formaldehyde: Pathways for reductive synthesis and energy storage, J. Green Chem. 19 (2017) 2347–2355. doi:10.1039/c6gc03093a.

[15] M.H. Peyrovi, N. Parsafard, H. Hasanpour, Catalytic Study of the Partial Oxidation Reaction of Methanol to Formaldehyde in the Vapor Phase, J. Bull. Chem. React. Eng. & Catal. 13 (2018) 520–528. doi:10.9767/bcrec.13.3.2048.520-528.

[16] H.Y. Kim, H.M. Lee, H. Metiu, Oxidative dehydrogenation of methanol to formaldehyde by a vanadium oxide cluster supported on rutile TiO_2(110): Which oxygen is involved ?, J. Phys. Chem. C. 114 (2010) 13736–13738. doi:10.1021/jp103361v.

[17] T.J. Yang, J.H. Lunsford, Partial Oxidation of Methanol to Formaldehyde Oxide on Silica over Molybdenum, J. Catal.103 (1987) 55–64.doi.org/10.1016/0021-9517(87)90092-3.

[18] N. Tabaja, S. Casale, D. Brouri, A. Davidson, H. Obeid, J. Toufaily, T. Hamieh, Comptes Rendus Chimie Quantum-dots containing Fe / SBA-15 silica as "' green '" catalysts for the selective photocatalytic oxidation of alcohol (methanol , under visible light), J. Comptes Rendus - Chim. 18 (2015) 358–367. doi:10.1016/j.crci.2015.01.010.

[19] K. Kočí, I. Troppová, M. Edelmannová, J. Starostka, L. Matějová, J. Lang, M. Reli, H. Drobná, A. Rokicińska, P. Kuśtrowski, L. Čapek, Photocatalytic decomposition of methanol over La/TiO_2 materials,J. Environ. Sci. Pollut. Res. 25 (2018) 34818–34825. doi:10.1007/s11356-017-0460-x.

[20] Q. Shi, G. Ping, X. Wang, H. Xu, J. Li, J. Cui, H. Abroshan, H. Ding, G. Li, CuO/TiO_2 heterojunction composites: An efficient photocatalyst for selective oxidation of methanol to methyl formate, J. Mater. Chem. A. 7 (2019) 2253–2260. doi:10.1039/c8ta09439j.

[21] S. Goldstein, D. Behar, J. Rabani, Mechanism of visible light photocatalytic oxidation of methanol in aerated aqueous suspensions of carbon-doped TiO_2, J. Phys. Chem. C. 112 (2008) 15134–15139. doi:10.1021/jp803974a.

[22] Q. Yuan, Z. Wu, Y. Jin, L. Xu, F. Xiong, Y. Ma, W. Huang, Photocatalytic cross-coupling of methanol and formaldehyde on a rutile TiO_2(110) surface, J. Am. Chem. Soc. 135 (2013) 5212–5219. doi:10.1021/ja400978r.

[23] T.S. Natarajan, H.C. Bajaj, R.J. Tayade, Enhanced direct sunlight photocatalytic oxidation of methanol using nanocrystalline TiO_2 calcined at different temperature, J. Nanoparticle Res. 16 (2014). doi:10.1007/s11051-014-2713-7.

[24] M. Reza, D. Khaki, M. Saleh, A. Aziz, A. Raman, W. Mohd, A. Wan, Application of doped photocatalysts for organic pollutant degradation - A review, J. Environ. Manage. 198 (2017) 78–94. doi:10.1016/j.jenvman.2017.04.099.

[25] X. Sun, H.-J. Li, N. Ou, B. Lyu, B. Gui, S. Tian, D. Qian, X. Wang, J. Yang, Visible-Light Driven TiO2 Photocatalyst Coated with Graphene Quantum Dots of Tunable Nitrogen Doping, J.Molecules. 24 (2019) 344. doi:10.3390/molecules24020344.

[26] J.L. Shi, H. Hao, X. Lang, Phenol-TiO_2 complex photocatalysis: Visible light-driven selective oxidation of amines into imines in air, Sustain. Energy Fuels. 3 (2019) 488–498. doi:10.1039/c8se00527c.

[27] M. Ai, W. Qin, T. Xia, Y. Ye, X. Chen, P. Zhang, Photocatalytic Degradation of 2,4-Dichlorophenol by TiO_2 Intercalated Talc Nanocomposite , Int. J. Photoenergy. 2019 (2019) 1–11. doi:10.1155/2019/1540271.

[28] U.I. Gaya, A.H. Abdullah, Heterogeneous photocatalytic degradation of organic contaminants over titanium dioxide: A review of fundamentals, progress and problems, J. Photochem. Photobiol. C Photochem. Rev. 9 (2008) 1–12. doi:10.1016/j.jphotochemrev.2007.12.003.

[29] Q. Xiang, B. Cheng, J. Yu, Graphene-Based Photocatalysts for Solar-Fuel Generation , Angew. Chem. Int. Ed.54 (2015) 11350–11366. doi:10.1002/anie.201411096.

[30] G.R. Surikanti, A.K. Bandarapu, M. V. Sunkara, A Facile One Pot Synthesis of $Cu_2O@TiO_2$: A Nanocomposite Catalyst for Enhanced Visible Light Driven J. Photocatalysis, Chem. Select. 4 (2019) 2249–2257. doi:10.1002/slct.201900003.

[31] W. Xie, R. Li, Q. Xu, Enhanced photocatalytic activity of Se-doped TiO_2 under visible light irradiation, J. Sci. Rep. 8 (2018) 1–10. doi:10.1038/s41598-018-27135-4.

[32] R. Asahi, T. Morikawa, H. Irie, T. Ohwaki, Nitrogen-Doped Titanium Dioxide as Visible-Light-Sensitive Photocatalyst : Designs , Developments , and Prospects, J. Chem. Rev. 114 (2014) 9824-9852. doi:10.1021/cr5000738.

[33] H. Tada, Q. Jin, A. Iwaszuk, M. Nolan, Molecular-scale transition metal oxide nanocluster surface-modified titanium dioxide as solar-activated environmental catalysts, J. Phys. Chem. C. 118 (2014) 12077–12086. doi:10.1021/jp412312m.

[34] J. Reszczyńska, T. Grzyb, J.W. Sobczak, W. Lisowski, M. Gazda, B. Ohtani, A. Zaleska, Visible light activity of rare earth metal doped (Er^{3+}, Yb^{3+} or Er^{3+}/Yb^{3+}) titania photocatalysts, Appl. Catal. B Environ. 163 (2015) 40–49. doi:10.1016/j.apcatb.2014.07.010.

[35] G. Murugadoss, R. Jayavel, M. Rajesh Kumar, Systematic investigation of structural and morphological studies on doped TiO_2nanoparticles for solar cell applications, J. Super lattices. Microstruct. 76 (2014) 349–361. doi:10.1016/j.spmi.2014.10.027.

[36] R. Long, N.J. English, Band gap engineering of double-cation-impurity-doped anatase-titania for visible-light photocatalysts : a hybrid density functional theory approach, J. Phys. Chem. Chem. Phys. 13 (2011) 13698–13703. doi:10.1039/c1cp21454c.

[37] D. Jiang, Y. Xu, D. Wu, Y. Sun, Visible light driven photocatalysis mediated via ligand-to-metal charge transfer (LMCT): an alternative approach to solar activation of titania, J. Solid State Chem. 181 (2008) 593–602. doi:10.1016/j.jssc.2008.01.004.

[38] C. Langhammer, Z. Yuan, I. Zorić, B. Kasemo, Plasmonic properties of supported Pt and Pd nanostructures, J. Nano Lett. 6 (2006) 833–838. doi:10.1021/nl060219x.

[39] J. Ran, J. Zhang, J. Yu, M. Jaroniec, S.Z. Qiao, Earth-abundant cocatalysts for semiconductor-based photocatalytic water splitting, J. Chem. Soc. Rev. 43 (2014) 7787–7812. doi:10.1039/c3cs60425j.

[40] S. Bai, L. Wang, X. Chen, J. Du, Y. Xiong, Chemically exfoliated metallic MoS2 nanosheets: A promising supporting co-catalyst for enhancing the photocatalytic performance of TiO_2 nanocrystals, J. Nano Res. 8 (2014) 175–183. doi:10.1007/s12274-014-0606-9.

[41] M. Janczarek, M. Endo, D. Zhang, K. Wang, E. Kowalska, Enhanced photocatalytic and antimicrobial performance of cuprous oxide/titania: The effect of titania matrix, J.Materials. 11 (2018) 2069. doi:10.3390/ma11112069.

[42] M. Lei, N. Wang, L. Zhu, Q. Zhou, G. Nie, H. Tang, Photocatalytic reductive degradation of polybrominated diphenyl ethers on CuO/TiO_2 nanocomposites: A mechanism based on the switching of photocatalytic reduction potential being controlled by the valence state of copper, J. Appl. Catal. B Environ. 182 (2016) 414–423. doi:10.1016/j.apcatb.2015.09.031.

[43] A.L. Luna, M. a. Valenzuela, C. Colbeau-Justin, P. Vázquez, J.L. Rodriguez, J.R. Avendaño, S. Alfaro, S. Tirado, A. Garduño, J.M. De La Rosa, Photocatalytic degradation of gallic acid over CuO-TiO_2 composites under UV/Vis LEDs irradiation, J.Appl. Catal. A Gen. 521 (2016) 140–148. doi:10.1016/j.apcata.2015.10.044.

[44] M. Khairy, W. Zakaria, Effect of metal-doping of TiO_2nanoparticles on their photocatalytic activities toward removal of organic dyes, Egypt. J. Pet. 23 (2014) 419–426. doi:10.1016/j.ejpe.2014.09.010.

[45] M. Beija, C.A.M. Afonso, Synthesis and applications of Rhodamine derivatives as fluorescent probes, J. Chem. Soci. 38 (2009) 2410-2433.doi:10.1039/b901612k.

[46] L. Sun, J.R. Bolton, Determination of the Quantum Yield for the Photochemical Generation of Hydroxyl Radicals in TiO_2 Suspensions , J. Phys. Chem. 100 (2002) 4127–4134. doi:10.1021/jp9505800.

[47] F.H. Hussein, A.F. Halbus, H. a. K. Hassan, W. a. K. Hussein, Photocatalytic degradation of bismarck brown G using irradiated ZnO in aqueous solutions, E-Journal Chem. 7 (2010) 540–544. doi:10.1155/2010/719674.

[48] F.H. Hussein, A.F. Halbus, Rapid decolorization of cobalamin, Int. J. Photoenergy. 2012 (2012) 1-9. doi:10.1155/2012/495435.

[49] H. Mcconnell, Effect of Polar Solvents on the Absorption Frequency of n→π Electronic Transitions, J. Chem. Phys. 20 (1952) 700–704. doi:10.1063/1.1700519.

[50] C. Sotelo-Vazquez, R. Quesada-Cabrera, M. Ling, D.O. Scanlon, A. Kafizas, P.K. Thakur, T.L. Lee, A. Taylor, G.W. Watson, R.G. Palgrave, J.R. Durrant, C.S. Blackman, I.P. Parkin, Evidence

and Effect of Photogenerated Charge Transfer for Enhanced Photocatalysis in WO3/TiO_2 Heterojunction Films: A Computational and Experimental Study, J. Adv. Funct. Mater. 27 (2017) 1–10. doi:10.1002/adfm.201605413.

[51] B.H. Toby, R-factors in Rietveld analysis : How good is good enough ?, Powder Diffraction (Cambridge University) 21 (2006) 67–70. doi:10.1154/1.2179804.

[52] A. Marcilla, A. Gomez-Siurana, M.M. José, F.J. Valdés, Comments on the Methods of Characterization of Textural Properties of Solids from Gas Adsorption Data, J. Adsorpt. Sci. Technol. 27 (2009) 69–84. doi:10.1260/026361709788921579.

[53] S. Ngamta, N. Boonprakob, N. Wetchakun, K. Ounnunkad, A facile synthesis of nanocrystalline anatase TiO_2 from $TiOSO_4$ aqueous solution, Materials Letters 105 (2013) 76–79. doi:10.1016/j.matlet.2013.04.064.

[54] Š. Jan, Š. Václav, S. Bakardjieva, L. Szatmary, Synthesis of spherical metal oxide particles using homogeneous precipitation of aqueous solutions of metal sulfates with urea, J. Powder. Techn.169 (2006) 33–40. doi:10.1016/j.powtec.2006.07.009.

[55] L. Ge, M. Xu, H. Fang, M. Sun, Preparation of TiO_2 thin films from autoclaved sol containing needle-like anatase crystals, J. Appl. Surf. Sci. 253 (2006) 720–725. doi:10.1016/j.apsusc.2005.12.162.

[56] B.D. Viezbicke, S. Patel, B.E. Davis, D.P. Birnie, Evaluation of the Tauc method for optical absorption edge determination: ZnO thin films as a model system, J. Phys. Status Solidi Basic Res. 252 (2015) 1700–1710. doi:10.1002/pssb.201552007.

[57] R. D. Shannon, C. T. Prewitt, Effective ionic radii and crystal chemistry, J. Inorg. Nucl.Chem. 32 (1970) 1427-1441.doi.org/10.1016/0022-1902(70)80629-7.

[58] D.M. Tobaldi, C. Piccirillo, N. Rozman, R.C. Pullar, M.P. Seabra, A.S. Škapin, P.M.L. Castro, J.A. Labrincha, Effects of Cu, Zn and Cu-Zn addition on the microstructure and antibacterial and photocatalytic functional properties of Cu-Zn modified TiO_2 nano-heterostructures, J. Photochem. Photobiol. A Chem.330 (2016) 44-54. doi:10.1016/j.jphotochem.2016.07.016.

[59] I.R. MacDonald, S. Rhydderch, E. Holt, N. Grant, J.M.D. Storey, R.F. Howe, EPR studies of electron and hole trapping in titania photocatalysts, J. Catal. Today. 182 (2012) 39–45. doi:10.1016/j.cattod.2011.08.039.

[60] L.M. Cárdenas, D.J. Brassington, B.J. Allan, H. Coe, Intercomparison of Formaldehyde Measurements in Clean and Polluted Atmospheres, J. Atmosph. Chem. 37 (2000) 53–80. doi.org/10.1023/A:1006383520819.

[61] L. Jing, B. Xin, F. Yuan, L. Xue, B. Wang, H. Fu, Effects of surface oxygen vacancies on photophysical and photochemical processes of Zn-doped TiO_2 nanoparticles and their relationships, J. Phys. Chem. B. 110 (2006) 17860–17865. doi:10.1021/jp063148z.

[62] M.S.P. Francisco, V.R. Mastelaro, P.A.P. Nascente, Activity and Characterization by XPS , HR-TEM , Raman Spectroscopy , and BET Surface Area of CuO / CeO_2 -TiO_2 Catalysts, J. Phys. Chem B.105 (2001) 10515–10522. doi.org/10.1021/jp0109675.

[63] R. T.Ako, P.Ekanayake, D. J. Young, et al, Evaluation of surface energy state distribution and bulk defect concentration in DSSC photoanodes based on Sn, Fe, and Cu doped TiO_2, J. Appl. Surf. Sci.351 (2015) 950-961.doi.org/10.1016/j.apsusc.2015.06.015.

[64] B. Bharti, S. Kumar, H. Lee, R. Kumar, Formation of oxygen vacancies and Ti^{3+} state in TiO_2 thin film and enhanced optical properties by air plasma treatment, J. Nat. Publ. Gr. (2016) 1–12. doi:10.1038/srep32355.

[65] M.S. Hamdy, R. Amrollahi, G. Mul, Surface Ti3+-containing (blue) titania: A unique photocatalyst with high activity and selectivity in visible light-stimulated selective oxidation, J. ACS. Catal. 2 (2012) 2641–2647. doi:10.1021/cs300593d.

[66] M. Mohamad, B.U. Haq, R. Ahmed, a. Shaari, N. Ali, R. Hussain, A density functional study of structural, electronic and optical properties of titanium dioxide: Characterization of rutile, anatase and brookite polymorphs, J. Mater. Sci. Semicond. Process. 31 (2015) 405–414. doi:10.1016/j.mssp.2014.12.027.

[67] C. Di Valentin, G. Pacchioni, A. Selloni, Origin of the different photoactivity of N-doped anatase and rutile TiO_2, Phys. Rev. B 70 (2004) 1–4. doi:10.1103/PhysRevB.70.085116.

[68] A.A. Al-kahtani, Photocatalytic Degradation of Rhodamine B Dye in Wastewater Using Gelatin / CuS / PVA Nanocomposites under Solar Light Irradiation, J. Biomat. Nanobiotech. 8 (2017) 66–82. doi:10.4236/jbnb.2017.81005.

[69] Ritika, M. Kaur, A. Umar, S.K. Mehta, S.K. Kansal, BiF 3 octahedrons: A potential natural solar light active photocatalyst for the degradation of Rhodamine B dye in aqueous phase, J. Mater. Res. Bull. 112 (2019) 376–383. doi:10.1016/j.materresbull.2018.12.031.

[70] L. Huang, W. Fang, Y. Yang, J. Wu, H. Yu, X. Dong, T. Wang, Z. Liu, B. Zhao, Three-dimensional MoO3 nanoflowers assembled with nanosheets for rhodamine B degradation under visible light, J. Mater. Res. Bull. 108 (2018) 38-45 doi:10.1016/j.materresbull.2018.08.036.

[71] Yoshio Nosaka and Atsuko-Y. Nosaka, Generation and Detection of Reactive Oxygen Species in Photocatalysis, Chem. Rev., 117, 17 (2017) 11302–11336. doi.org/10.1021/acs.chemrev.7b00161

Graphical abstract :